Performance Analysis of IRS-Assisted Multi-Link FSO System Under Pointing Errors

Takumi Ishida , *Graduate Student Member, IEEE*, Chedlia Ben Naila , *Senior Member, IEEE*,
Hiraku Okada , *Member, IEEE*, and Masaaki Katayama , *Senior Member, IEEE*

Abstract—The integration of intelligent reflecting surfaces (IRS) into free-space optical (FSO) communication systems is considered as a promising and innovative approach to overcoming existing challenges due to the strict line-of-sight (LoS) requirements faced by conventional FSO setups, thereby ensuring more flexible and controllable links and expanding the communication coverage area. Nonetheless, the configuration of IRS-assisted FSO systems remains relatively novel, requiring investigation into optimizing IRS placement to enhance system performance while mitigating interference and obstacles in dynamic environmental conditions. This work aims to evaluate the improvement of the system performance achieved through optimized IRS positioning while accounting for the main degrading factors inherent in FSO systems and IRS design. We present a comprehensive model for a multilink terrestrial IRS-assisted FSO system, taking into consideration key degrading factors such as pointing errors stemming from both transmitter and IRS jitter, IRS dimensions, and turbulence-induced fading. Furthermore, we derive closed-form expressions for the probability density function of channel coefficients, average bit error rate, and outage probability. Our results indicate that optimal IRS placement is in proximity to the transmitter, taking into account all channel impairments. Furthermore, we showed that optimal IRS placement tends to shift towards the receiver side as the IRS jitter increases. Consequently, the analysis presented offers valuable insights for efficiently designing IRS-assisted FSO systems, particularly regarding IRS placement in the presence of pointing errors.

Index Terms—Atmospheric turbulence, beam jitter, free-space optics, intelligent reflecting surfaces, pointing error.

I. INTRODUCTION

FREE space optics (FSO) communication emerges as a promising technology for next-generation communications due to its capability of high data rates and cost-effective transmission [1]. Unlike traditional radio frequency (RF) communication, FSO systems operate within a wide spectrum and are resilient to electromagnetic interference. FSO has been recognized as a cost-effective solution for backhaul for wireless cellular

networks [2], terrestrial fiber backup [3], applications for beyond 5G and 6G networks, and disaster recovery scenarios [4].

However, the propagation of the optical beams through the atmosphere is affected by different degrading factors due to the nature of the light, including attenuation, atmospheric turbulence [5], [6], [7], and pointing errors [8]. Furthermore, communication through FSO links requires a direct line-of-sight (LoS) link between the transmitter (Tx) and receiver (Rx). To tackle these challenges, several approaches have been proposed, including the use of multiple-input multiple-output (MIMO) configuration [9] and hybrid RF/FSO systems [10]. Moreover, optical relay nodes [11] have been implemented as an effective solution for the LoS problem, although their deployment is costly and challenging due to the need for extensive additional hardware. Instead, the emerging technology of intelligent reflecting surfaces (IRS) is anticipated to offer a solution to this issue [12], [13]. The IRS efficiently redirects incoming beams without the complexity of relay systems, operating passively with minimal power requirements [14].

Driven by the potential of IRS, research works have extensively been carried out on their applications and implementations [15], [16], [17], [18], [19], [20], [21], [22], [23], [24]. In [15], the modeling and design aspects of an IRS-assisted FSO system were investigated, considering the Huygens-Fresnel principle and presenting sharing protocols tailored for optical IRS setups. The authors in [16] introduced a controllable multibranch optical wireless communication system leveraging an optical IRS, addressing factors such as beam jitter, IRS jitter, and obstruction probability. Moreover, an analytical model for geometric and misalignment loss was presented in [17], which incorporates random statistical modeling of incident and reflection angles of transmitted laser beams, yielding closed-form expressions. In [18], The authors presented a phase-shift design for an IRS aimed at beam focusing, specifically when the beam width is comparable to or smaller than the aperture size. In [19], the authors assessed an IRS-assisted unmanned aerial vehicle relay system in a hybrid FSO/RF satellite-to-ground network, considering the effects of atmospheric turbulence and hovering-induced pointing errors. Whereas a hybrid RF/IRS system was investigated, taking into account the physical models of optical IRS and the RF channel simultaneously [20]. Moreover, the cascaded multiple IRS-equipped Mixed FSO-RF system was investigated, taking into generalized fading channels [21]. Regarding cascaded system, statistically characterized cascaded composite turbulence and misalignment channels were

presented [22]. In [23], an optical IRS-assisted MIMO FSO system was introduced based on the optical space shift keying technique, revealing a trade-off between average bit error rate (BER) performance and spectral efficiency. The authors in [24] evaluated the ergodic channel capacity of multiple-input single-output (MISO) FSO communication systems by exploiting the hollow of concave reflectors to focus the reflected beams on a single user.

Despite several research works aforementioned, only a few have investigated the placement of IRS, taking into account factors such as the link distance between the Tx and IRS, as well as their orientation and altitude [25], [26], [27]. While the authors in [25] evaluated IRS placement, they focused solely on geometric loss, neglecting the potential impact of random misalignment caused by building sway. In [26], optical IRSs were compared with optical relays across different power scaling regimes, focusing on outage probability, diversity and coding gains, and optimal placement. In [27], it has been shown that the outage probability of IRS-assisted FSO systems fluctuates based on IRS placement. Nonetheless, the authors only accounted for the distance between the Tx and the IRS and the jitter of a building-mounted IRS without considering realistic factors such as the incident angle to the IRS or the IRS size.

In this work, we propose to investigate the influence of IRS placement on an IRS-assisted multilink FSO system and determine an optimal placement for the IRS to improve the overall performance. We introduce a comprehensive framework to evaluate system performance, considering key factors such as attenuation, atmospheric turbulence, and pointing errors. Additionally, we examine the effects of the IRS jitter angle and inherent losses due to IRS size. Within our proposed framework, we incorporate considerations for incident and reflection angles. Moreover, we evaluate how incident angle and IRS size affect IRS placement and investigate the relationship between pointing errors, specifically random misalignment and IRS placement.

The structure of the paper is as follows: Section II introduces the proposed system configuration and the channel model. We summarize and discuss the numerical results in Section III. Finally, Section IV provides the conclusion of the paper.

II. SYSTEM MODEL

We consider a FSO system incorporating an IRS to facilitate the redirection of optical signals from the Tx to the Rx when a direct LoS is obstructed by various obstacles, as illustrated in Fig. 1. Positioned atop a building, the IRS module acts as a reflective interface for incoming signals, redirecting them toward the Rx. We assume similar atmospheric turbulence and attenuation effects on both optical sub-channels, from Tx-to-IRS and IRS-to-Rx. In this setup, the received optical signal power at the Rx is mainly affected by pointing errors resulting from beam jitter originating from the Tx, jitter of the IRS, and fading in both sub-channels. The IRS comprises N elements, while both the Tx and Rx are multi-aperture devices. Each element of the IRS reflects optical beams toward the Rx. It is assumed that each IRS element precisely reflects each optical beam without any interference.
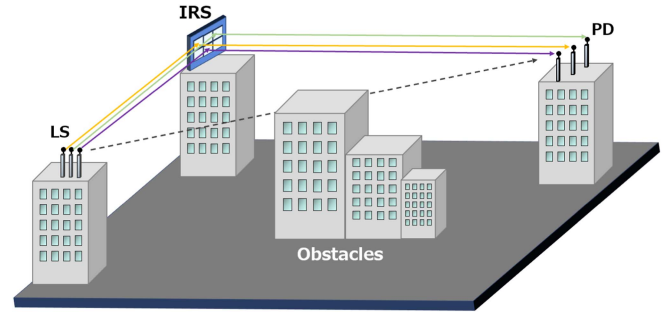

Fig. 1. System configuration of multi-link terrestrial IRS-assisted FSO system.

As shown in the system illustrated in Fig. 2, the received electrical signal at the k-th intelligent channel, denoted as r_k, can be expressed as

$$r_k = \xi \, \eta \, h_k \, p_k + n_k, \qquad (1)$$

where ξ is the attenuation coefficient introduced by the IRS, η corresponds to the responsivity of the photodetector, p_k takes on values of either 0 or $2P_t$, where P_t is the average power of the transmitted signal. The variable n_k denotes additive white Gaussian noise (AWGN) at the Rx with a zero mean and a variance of σ_N^2 and h_k represents the channel fading, as expressed by

$$h_k = h_a h_t h_p h_{irs}, \qquad (2)$$

where h_a and h_{irs} denote the deterministic channel fading resulting from attenuation and IRS size limitations, respectively. h_t and h_p represent the channel fading due to atmospheric turbulence and pointing errors, respectively. The fading in h_a and h_p follows random distributions.

A. Attenuation

As a laser beam travels through the atmosphere, it undergoes absorption and scattering by particles, resulting in attenuation, which is defined as [28]

$$h_a = \exp\left(-\epsilon(L_1 + L_2)\right), \qquad (3)$$

where the attenuation factor, denoted by $\epsilon(\lambda)$, is expressed as $\frac{3.912}{V}\left(\frac{\lambda}{550}\right)^{-q}$ and accounts for the absorption and scattering of the laser beam, with a dependency on wavelength. V represents visibility, and λ is the wavelength. Tx-to-IRS and IRS-to-Rx distances are denoted as L_1 and L_2, respectively. The parameter q is set to 1.3 when the visibility falls within the range of 6 km < V < 50 km, as specified by the Kim model [6].

B. Atmospheric Turbulence

Optical transmission through FSO links is predominantly affected by atmospheric turbulence, resulting from spatially and randomly fluctuating air temperatures. To quantify these scintillation effects, we utilized the extensively employed Gamma-Gamma fading model, applicable across a spectrum of turbulence strengths. The probability density function (PDF) of h_a, representing these turbulence effects, can be expressed as
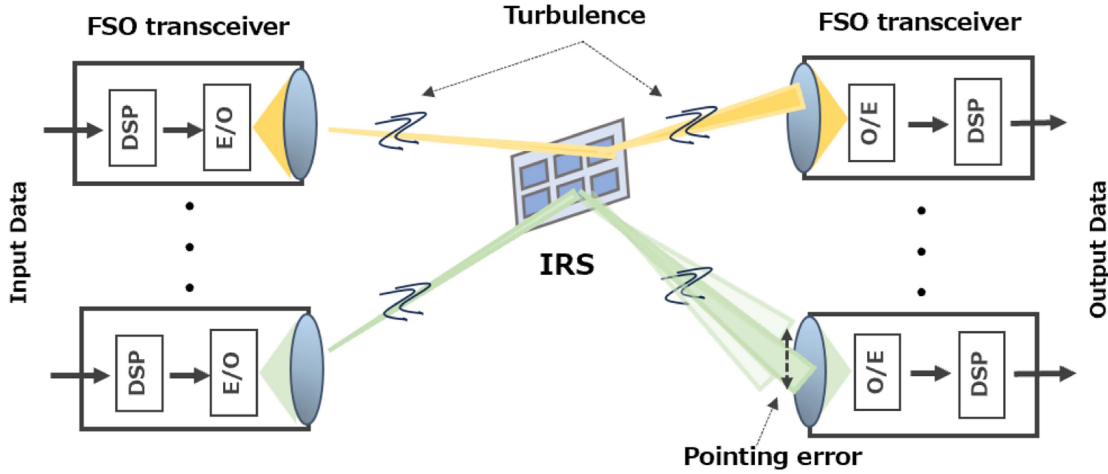
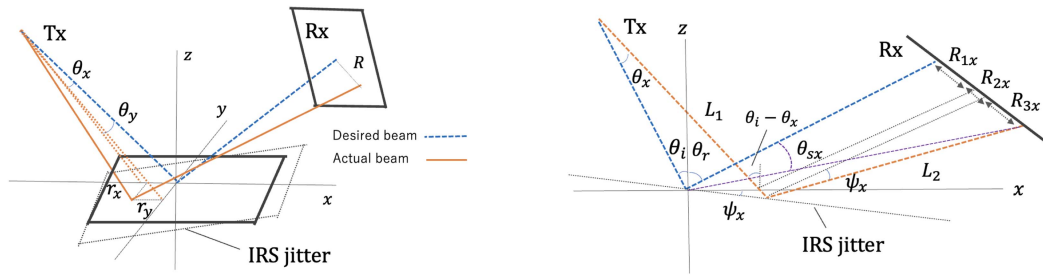Fig. 2. Block diagram of multi-link terrestrial IRS-assisted FSO system.

(a) Light path between Tx and Rx via IRS considering Tx and IRS jitter.

(b) Displacement of the beam due to the Tx and IRS jitters on the xz plane

Fig. 3. Pointing error due to the Tx and IRS jitters.

follows [28]

$$f(h_t) = \frac{2(\alpha\beta)^{\frac{(\alpha+\beta)}{2}}}{\Gamma(\alpha)\Gamma(\beta)} h_t^{\frac{(\alpha+\beta)}{2}-1} K_{\alpha-\beta}\left(2\sqrt{\alpha\beta h_t}\right), \quad (4)$$

where $\Gamma[\cdot]$ represents the Gamma function, and $K_v(\cdot)$ stands for the v-th order modified Bessel function of the second kind. The parameters α and β characterize the large-scale scattering and small-scale fading, respectively. These parameters can be expressed under the plane wave approximation [28]

$$\alpha = \left[\exp\left(\frac{0.49\sigma_R^2}{(1+1.11\sigma_R^{12/5})^{7/6}}\right) - 1\right]^{-1}, \quad (5)$$

$$\beta = \left[\exp\left(\frac{0.51\sigma_R^2}{(1+0.69\sigma_R^{12/5})^{5/6}}\right) - 1\right]^{-1}, \quad (6)$$

where $\sigma_R^2 = 1.23 C_n^2 k^{7/6}(L_1 + L_2)^{11/6}$ denotes the Rytov variance [29], with C_n^2 being the refractive index structure parameter that serves as an indicator of turbulence strength. a represents the Rx radius and $k = 2\pi/\lambda$ denotes the wave number.

C. Pointing Errors

In LoS-FSO communication, FSO systems necessitate ongoing alignment between the Tx and Rx to guarantee reliability and optimal performance. Nonetheless, achieving and maintaining this alignment can pose challenges, particularly in the presence of unpredictable building sways induced by factors such as wind loads and thermal expansions. Furthermore, in IRS-assisted FSO systems, the pointing errors must consider the beam offset introduced by the IRS jitter. As shown in Fig. 3(a), the IRS is initially positioned at the center of the xy plane in the absence of jitter, with the z axis perpendicular to the IRS center. The reflected beam from the IRS aligns perpendicularly with the Rx. Displacements in the x and y directions are represented as r_x and r_y, respectively.

We assume that the beam displacements in the x direction (θ_x) and the y direction (θ_y) follow Gaussian distributions with a mean of zero and a variance of σ_θ^2. Furthermore, we consider the center of the IRS as the reference point for jitter. The jitter of the IRS in the x direction (ψ_x) and the y direction (ψ_y) is assumed to follow Gaussian distributions with a mean of zero and a variance of σ_ψ^2.

Fig. 3(b) depicts the displacement at the Rx on the xz plane, where the total beam offset is represented as $R_{1x} + R_{2x} + R_{3x}$.

Assuming that the Tx jitter θ_x is sufficiently small, the approximation for R_{1x} reads

$$R_{1x} = \frac{\sin(90 - \theta_r)}{\sin(90 - \theta_i - \theta_x)} L_1 \tan \theta_x$$

$$\approx \frac{\cos \theta_r}{\cos \theta_i} L_1 \theta_x. \tag{7}$$

On the other hand, with the IRS jitter ψ_x considered to be sufficiently small, we neglect R_{2x}. Under the assumption of negligible IRS jitter ψ_x, the approximation for R_{3x} is given by

$$R_{3x} = \frac{L_2}{\tan(90 - \theta_x - 2\psi_x)}$$

$$\approx (\theta_x + 2\psi_x) L_2. \tag{8}$$

The angle θ_{sx}, including both the Tx jitter and IRS jitter, can be expressed as

$$\theta_{sx} = \frac{R_{1x} + R_{3x}}{L_2}$$

$$= \frac{\cos \theta_r}{\cos \theta_i} \frac{L_1}{L_2} \theta_x + \psi_x. \tag{9}$$

Up to this point, we have conducted calculations in the x direction; however, the same computation can also be performed in the y direction. The overall angle θ_s is composed of both θ_{sx} and θ_{sy} and can be written as

$$\theta_s^2 = \theta_{sx}^2 + \theta_{sy}^2. \tag{10}$$

Since θ_{sx} and θ_{sy} are independent and identically distributed, θ_s follows a Rayleigh distribution. Consequently, the PDF of θ_s can be expressed as

$$f_{\theta_s}(\theta_s) = \frac{\theta_s}{(\frac{\cos \theta_r}{\cos \theta_i} \frac{L_1}{L_2})^2 \sigma_\theta^2 + \sigma_\psi^2}$$

$$\times \exp\left(-\frac{\theta_s^2}{2(\frac{\cos \theta_r}{\cos \theta_i} \frac{L_1}{L_2})^2 \sigma_\theta^2 + 2\sigma_\psi^2}\right). \tag{11}$$

The distance from the center of the Rx to the receiving light spot, denoted as R, can be represented as [16]

$$R = \tan \theta_s L_2 \approx \theta_s L_2. \tag{12}$$

The channel fading resulting from pointing error, denoted as h_p, can be approximated as [8]

$$h_p \approx A_0 \exp\left(\frac{-2R^2}{w_{z_{eq}}^2}\right), \tag{13}$$

$$w_{z_{eq}}^2 = \frac{w_z^2 \sqrt{\pi} \text{erf}(v)}{2v \exp(-v^2)}, \tag{14}$$

$$v = \sqrt{\pi} a / \sqrt{2} w_z, \tag{15}$$

where A_0 denotes the fraction of received optical power collected at $R = 0$ and is defined as $A_0 = [\text{erf}(v)]^2$. The approximation provided by (13) holds true when $w_z / a > 6$, with w_z being the beam width [8].

By substituting (12) and (13) into (11), the PDF of h_p can be derived as

$$f_{h_p}(h_p) = f_{\theta_s}(\theta_s) \left| \frac{d\theta_s}{dh_p} \right|$$

$$= \frac{\rho}{A_0} \left(\frac{h_p}{A_0}\right)^{\rho - 1}, \quad 0 \leq h_p \leq A_0, \tag{16}$$

where

$$\rho = \frac{w_{z_{eq}}^2}{4(\frac{\cos \theta_r}{\cos \theta_i})^2 \sigma_\theta^2 L^2 + 16\sigma_\psi^2 L_2^2}. \tag{17}$$

D. Transmit Diversity Due to IRS Size

Assuming the IRS is sufficiently large for reflecting the beam, the beam width can be simply expressed as

$$w_z = \phi(L_1 + L_2), \tag{18}$$

where ϕ represents the beam divergence.

However, the beam width is limited by the size of the IRS, as it can only reflect the beam within its specific area. Consequently, the beam width at the receiver (Rx) is given by

$$w_z = \begin{cases} l + \phi L_2, & w_z \geq l \\ w_{irs} + \phi L_2, & otherwise \end{cases} \tag{19}$$

where l is the length of the IRS. The beam width at the IRS denoted as w_{irs}, can be determined by

$$w_{irs} = \phi L_1. \tag{20}$$

In our work, we take into account the beam divergence at the IRS. It should be noted that the pointing error (13) incorporates the beam divergence at the Rx. To simplify the calculations, we adopt two assumptions: firstly, that the beam has a circular shape, and secondly, that the power of the beam is uniformly distributed across the beam spot.

The area of the beam spot size S is derived as

$$S = \frac{\pi w_{irs}^2}{4 \cos \theta_i}. \tag{21}$$

The total area of elements, S_{irs}, that reflect the optical beams can be expressed as

$$S_{irs} = \sum_{m=1}^{M} \sum_{n=1}^{M} z_m \times z_n \quad S \in (m, n), \tag{22}$$

where $z_m \times z_n$ is the area of one IRS element, and M^2 represents the number of IRS elements on the beam spot.

Subsequently, the ratio of power that can be reflected by the IRS is as follows

$$h_{irs} = \frac{S_{irs}}{S}. \tag{23}$$

E. Channel Fading

The PDF of the optical channel fading from the Tx to the Rx, denoted as $h = h_a h_{irs} h_t h_p$, can be determined by

$$f_h(h) = \int_{-\infty}^{\infty} f_{h_t}(h_t) f_{h_p}\left(\frac{h}{h_t h_a h_{irs}}\right) \frac{1}{h_t h_a h_{irs}} dh_t. \quad (24)$$

By substituting (4) and (16) into (24), the PDF of h can be derived as

$$f_h(h) = \frac{2\rho(\alpha\beta)^{\frac{\alpha+\beta}{2}}}{A_0^\rho h_a^\rho h_{irs}^\rho \Gamma(\alpha)\Gamma(\beta)} h^{\rho-1}$$

$$\times \int_{h/A_0 h_a h_{irs}}^{\infty} h_t^{(\alpha+\beta)/2-1-\rho} K_{\alpha-\beta}(2\sqrt{\alpha\beta h_t}) \, dh_t. \quad (25)$$

The modified Bessel function of the second kind can be rewritten in terms of Meijer's G-function.

$$K_v(x) = \frac{1}{2} G_{0,2}^{2,0}\left[\frac{x^2}{4} \,\middle|\, \begin{matrix} - \\ v/2 & -v/2 \end{matrix}\right]. \quad (26)$$

Furthermore, by applying [30, (07.34.21.0085.01)], we obtain a closed-form expression as follows

$$f_h(h) = \frac{\alpha\beta\rho}{A_0 h_a h_{irs}\Gamma(\alpha)\Gamma(\beta)}$$

$$\times G_{1,3}^{3,0}\left[\frac{\alpha\beta h}{A_0 h_a h_{irs}} \,\middle|\, \begin{matrix} \rho \\ \rho-1 & \alpha-1 & \beta-1 \end{matrix}\right]. \quad (27)$$

The instantaneous electrical signal-to-noise ratio (SNR) can be expressed as

$$\gamma = \frac{(\sum_{k=1}^N h_k)^2 P_t^2 \xi^2 \eta^2}{\sigma_n^2}$$

$$= \overline{\gamma}\left(\sum_{k=1}^N h_k\right)^2, \quad (28)$$

where $\overline{\gamma} = P_t^2 \xi^2 \eta^2 / \sigma_n^2$ denotes the SNR under the assumption of no channel impairments in the channel.

We assume that the channel coefficient $h_1, h_2, \ldots h_n$ are $h = h_1 = h_2 = \ldots = h_n$. Therefore, the electrical SNR can be expressed as

$$\gamma = \overline{\gamma} N^2 h^2. \quad (29)$$

Using the Jacobian random variable transformation method, we can derive the PDF of the SNR as follows

$$f_\gamma(\gamma) = f_h\left(\sqrt{\frac{\gamma}{\overline{\gamma} N^2}}\right)\left|\frac{dh}{d\gamma}\right|. \quad (30)$$

By substituting (27) into (30), we obtain

$$f_\gamma(\gamma) = \frac{\alpha\beta\rho}{2\sqrt{\gamma\overline{\gamma}} A_0 h_a h_{irs} N\Gamma(\alpha)\Gamma(\beta)} \times G_{1,3}^{3,0}$$

$$\left[\frac{\alpha\beta}{A_0 h_a h_{irs} N}\sqrt{\frac{\gamma}{\overline{\gamma}}} \,\middle|\, \begin{matrix} \rho \\ \rho-1 & \alpha-1 & \beta-1 \end{matrix}\right]. \quad (31)$$

F. Bit-Error Rate

We obtain the BER for intensity modulation and direct detection (IM/DD) employing on-off keying (OOK) in the presence of AWGN. Considering that the average BER is defined as the statistical average value of the instantaneous error probability over all possible channel states, it can be determined by averaging (31) over the PDF of γ, as follows

$$P_e = \int_0^\infty Q(\sqrt{\gamma}) f_\gamma(\gamma) d\gamma, \quad (32)$$

where $Q(\cdot)$ denotes the Gaussian Q-function, which is connected to the complementary error function $\mathbf{erfc}(\cdot)$ through the relationship $\mathbf{erfc}(x) = 2Q(\sqrt{2}x)$.

By substituting (31) into (32), the average BER can be derived as

$$P_e = \int_0^\infty \frac{\alpha\beta\rho}{2\sqrt{\gamma\overline{\gamma}} A_0 h_a h_{irs} N\Gamma(\alpha)\Gamma(\beta)} \mathbf{erfc}\left(\sqrt{\frac{\gamma}{2}}\right)$$

$$\times G_{1,3}^{3,0}\left[\frac{\alpha\beta}{A_0 h_a h_{irs} N}\sqrt{\frac{\gamma}{\overline{\gamma}}} \,\middle|\, \begin{matrix} \rho \\ \rho-1 & \alpha-1 & \beta-1 \end{matrix}\right] d\gamma. \quad (33)$$

To solve (33), we expressed $\mathbf{erfc}(x)$ in terms of Meijer's G-function, i.e.,

$$\mathbf{erfc}(\sqrt{x}) = \frac{1}{\sqrt{\pi}} G_{1,2}^{2,0}\left[x \,\middle|\, \begin{matrix} 1 \\ 0 & 1/2 \end{matrix}\right]. \quad (34)$$

By applying equations [31, (9.31.1)] and [32, (21)] in (33), we obtain a closed-form expression for the average BER as follows

$$P_e = \frac{\alpha\beta\rho 2^{\alpha+\beta-\frac{13}{2}}}{\pi\sqrt{\overline{\gamma}} A_0 h_a h_{irs} N\Gamma(\alpha)\Gamma(\beta)}$$

$$\times G_{4,7}^{6,2}\left[\frac{\alpha^2\beta^2}{8A_0^2 h_a^2 \, h_{irs}^2 \overline{\gamma} N^2} \,\middle|\, \right.$$

$$\left. \begin{matrix} \frac{1}{2} & 0 & \frac{\rho}{2} & \frac{\rho+1}{2} \\ \frac{\rho-1}{2} & \frac{\rho}{2} & \frac{\alpha-1}{2} & \frac{\alpha}{2} & \frac{\beta-1}{2} & \frac{\beta}{2} & -\frac{1}{2} \end{matrix}\right]. \quad (35)$$

Similar to (35), the average BER without pointing errors can be expressed as

$$P_e' = \frac{2^{\alpha+\beta-4}}{\pi\sqrt{\overline{\gamma}} N\Gamma(\alpha)\Gamma(\beta)} \times G_{2,5}^{4,2}$$

$$\left[\frac{\alpha^2\beta^2}{8A_0^2 h_a^2 \, h_{irs}^2 \overline{\gamma} N^2} \,\middle|\, \begin{matrix} \frac{1}{2} & 0 \\ \frac{\alpha}{2} & \frac{\alpha+1}{2} & \frac{\beta}{2} & \frac{\beta+1}{2} & -\frac{1}{2} \end{matrix}\right]. \quad (36)$$

G. Outage Probability

The outage probability, defined as the probability of the instantaneous SNR γ falling below a specified SNR threshold γ_{th}, can be calculated by

$$P_{out} = Pr(\gamma \leq \gamma_{\text{th}})$$

$$= \int_0^{\gamma_{\text{th}}} f(\gamma) d\gamma$$

$$= F(\gamma_{\text{th}}), \quad (37)$$

where $F(\cdot)$ represents cumulative distribution function(CDF).

By substituting (31) into (37) and using [30, (07.34.21.0084.01)], the outage probability can be derived as

$$P_{out} = \frac{\alpha\beta\rho 2^{\alpha+\beta-5}\sqrt{\gamma_{th}}}{\pi\sqrt{\overline{\gamma}}A_0 h_a h_{irs}N\Gamma(\alpha)\Gamma(\beta)}$$

$$\times G_{3,7}^{6,1}\left[\frac{\alpha^2\beta^2\gamma_{th}}{16A_0^2 h_a^2\ h_{irs}^2\overline{\gamma}N^2}\right|$$

$$\left.\begin{matrix}\frac{1}{2} & \frac{\rho}{2} & \frac{\rho+1}{2} \\ \frac{\rho-1}{2} & \frac{\rho}{2} & \frac{\alpha-1}{2} & \frac{\alpha}{2} & \frac{\beta-1}{2} & \frac{\beta}{2} & -\frac{1}{2}\end{matrix}\right]. \quad (38)$$

Similar to (38), we obtain the outage probability without pointing errors as follows,

$$P'_{out} = \frac{2^{\alpha+\beta-2}\sqrt{\gamma_{th}}}{\pi N\Gamma(\alpha)\Gamma(\beta)}\times G_{1,5}^{4,1}$$

$$\left[\frac{\alpha^2\beta^2\gamma_{th}}{16h_a^2\ h_{irs}^2\overline{\gamma}N^2}\right|\left.\begin{matrix}\frac{1}{2} \\ \frac{\alpha}{2} & \frac{\alpha+1}{2} & \frac{\beta}{2} & \frac{\beta+1}{2} & -\frac{1}{2}\end{matrix}\right]. \quad (39)$$

H. Asymptotic Analysis

Using the technique presented in [33], we derived a closed-form expression of the asymptotic average BER at high SNR given by

$$P''_e \approx \left(\frac{\alpha\beta}{A_0 h_l h_{irs}n}\right)^{\Omega}\frac{\rho\Gamma(|\alpha-\beta|)\Gamma\left(\frac{\Omega+1}{2}\right)\overline{\gamma}^{-\frac{\Omega}{2}}}{(\rho-\Omega)2\sqrt{\pi}\Gamma(\Omega)\Gamma(\Omega+1)},\quad \rho>\Omega, \tag{40}$$

$$P''_e \approx \left(\frac{\alpha\beta}{A_0 h_l h_{irs}n}\right)^{\rho}\frac{\Gamma(\alpha-\rho)\Gamma(\beta-\rho)\Gamma\left(\frac{\rho+1}{2}\right)\overline{\gamma}^{-\frac{\Omega}{2}}}{2\sqrt{\pi}\Gamma(\alpha)\Gamma(\beta)},\quad \rho<\Omega, \tag{41}$$

where $\Omega = \min\{\alpha,\beta\}$.

A closed-form expression of the asymptotic outage probability is calculated in the same way as the asymptotic expression of the average BER.

$$P''_{out} \approx \left(\frac{\alpha\beta}{A_0 h_l h_{irs}n}\right)^{\Omega}\frac{\Gamma(|\alpha-\beta|)\Gamma\left(\frac{\Omega+1}{2}\right)\gamma_{th}^{\frac{\Omega}{2}}}{(\rho-\Omega)\Gamma(\Omega)\Gamma(\Omega+1)\overline{\gamma}^{\frac{\Omega}{2}}},\quad \rho>\Omega, \tag{42}$$

$$P''_{out} \approx \left(\frac{\alpha\beta}{A_0 h_l h_{irs}n}\right)^{\rho}\frac{\Gamma(\alpha-\rho)\Gamma(\beta-\rho)\Gamma\left(\frac{\rho+1}{2}\right)\gamma_{th}^{\frac{\Omega}{2}}}{(\Gamma(\alpha)\Gamma(\beta)\overline{\gamma}^{\frac{\Omega}{2}}},\quad \rho<\Omega, \tag{43}$$

III. NUMERICAL RESULTS

In this section, we present the performance results of the average BER and outage probability of the IRS-assisted FSO system, taking into account the collective impact of channel impairments such as atmospheric turbulence and pointing error. The derived theoretical results are validated through simulations across different parameters. We compare the numerical results with those obtained when there is no pointing error (PE). The numerical parameters are summarized in Table I. A refractive index structure parameter of $C_n^2 = 1\times 10^{-13}$ is employed to characterize strong atmospheric turbulence conditions. In the considered IRS configuration, the different elements are each

TABLE I
SYSTEM PARAMETERS

| Parameters	Symbols	Values
Tx-to-IRS distance	L_1	250 m
IRS-to-Rx distance	L_2	250 m
Visibility	V	10 km
Noise variance	σ_N^2	10^{-14} W/Hz
Incident angle	θ_i	$\pi/6$ rad
Reflection angle	θ_r	$\pi/6$ rad
Pointing error angle standard deviation	σ_θ	1×10^{-3} rad
IRS jitter angle standard deviation	σ_ψ	1×10^{-3} rad
PD's responsivity	η	0.8 A/W
Refractive index structure parameter	C_n^2	10^{-13} m$^{-2/3}$
Optical path-loss	h_l/L	0.2 dB/km
Optical wavelength	λ	1550 nm
IRS attenuation coefficient	ξ	0.95
Transmit divergence at $1/e^2$	ϕ	4×10^{-3} rad
Receiver radius	a	0.1 m
Transmitted optical power	P_t	20 dBm
SNR threshold	γ_{th}	5 dB
Number of IRS elements	N	64
IRS area	l^2	0.5×0.5 m^2
IRS element size	$z_m\times z_n$	0.01×0.01 m^2
IRS space between adjacent elements	z_a	2 cm
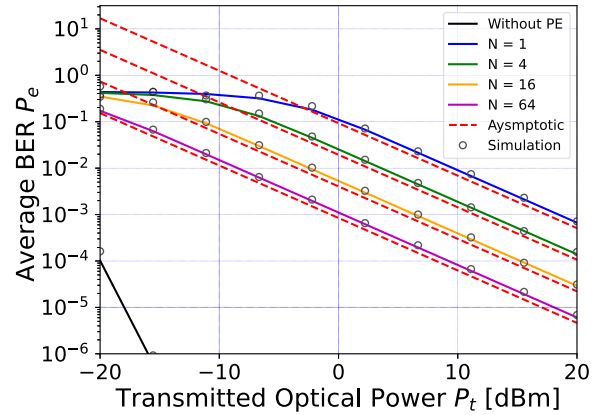
Fig. 4. Average BER in terms of transmitted optical power for different numbers of IRS reflecting elements.

sized at 1 cm^2, with a 2-cm separation between adjacent elements [12].

Fig. 4 shows the average BER as a function of transmitted optical power for different numbers of IRS reflecting elements. Notably, we observe improved performance with increasing transmitted optical power. Specifically, an average BER of $P_e = 10^{-2}$ is obtained with a single link ($N = 1$) while achieving an average BER of $P_e = 10^{-3}$ requires an IRS of 16 reflecting elements at a transmitted optical power of $P_t = 10$ dBm. As expected, the average BER consistently decreases by approximately the same factor each time the number of IRS elements quadruples. The use of a multi-link IRS-assisted FSO system enhances system performance.

Fig. 5 illustrates the average BER with respect to transmitted optical power for different IRS sizes, namely, 0.03 m $\times$ 0.03 m, 0.07 m $\times$ 0.07 m, 0.5 m $\times$ 0.5 m, and 1 m $\times$ 1 m. As the IRS size increases, there is an enhancement in system performance. The channel coefficient corresponding to different IRS sizes is as follows: $h_{irs} = 0.00012$ for $l^2 = 0.03$ m $\times$ 0.03 m, $h_{irs} = 0.00063$ for $l^2 = 0.07$ m $\times$ 0.07 m, $h_{irs} = 0.035$ for $l^2 = 0.5$ m $\times$ 0.5 m, and $h_{irs} = 0.11$ for $l^2 = 1$ m $\times$ 1 m. This indicates that smaller IRS sizes lead to the capture of relatively

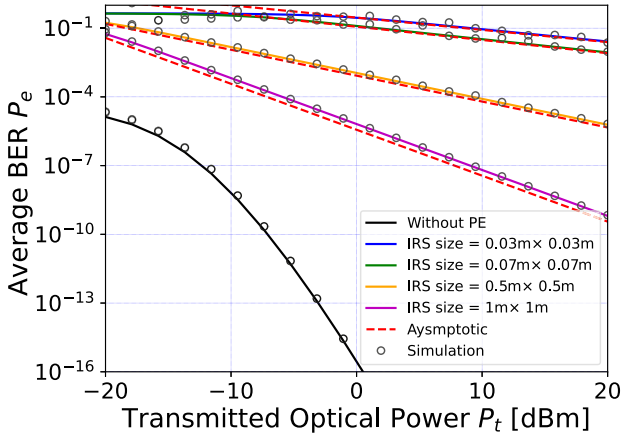Fig. 5. Average BER in terms of transmitted optical power for different IRS size.
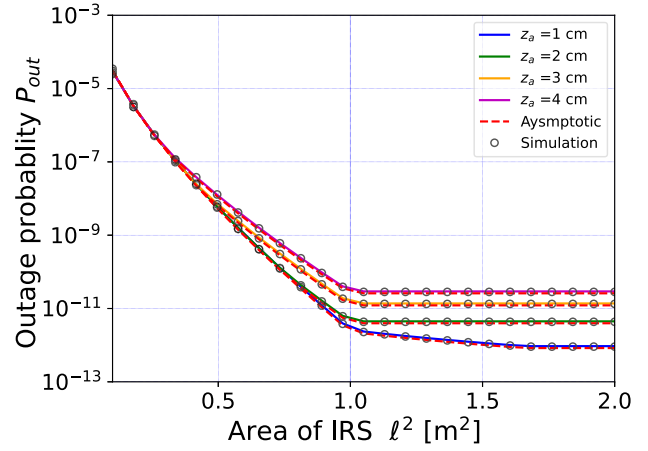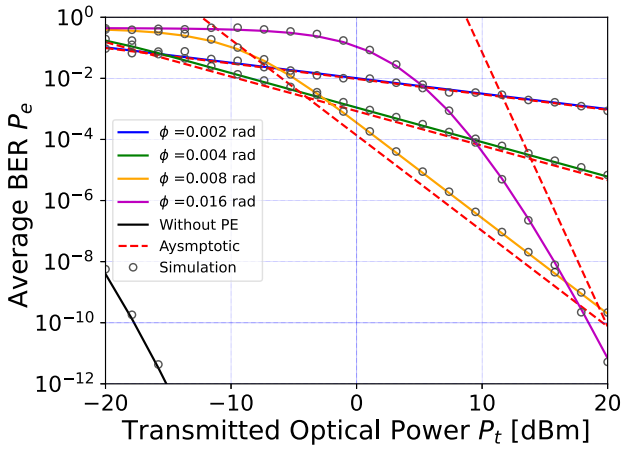

Fig. 6. Average BER in terms of transmitted optical power for different values of initial beam width.

Fig. 7. Average BER in terms of area of IRS for different beam divergence angles.

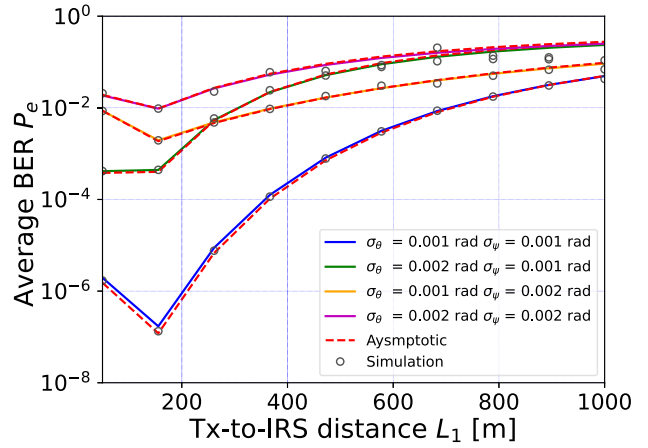Fig. 8. Outage probability in terms of area of IRS for different IRS space between adjacent elements.

Fig. 9. Average BER in terms of the Tx-to-IRS distance for different Tx and IRS jitters when IRS-to-Rx distance of 250 m and equal incident and reflection angles.
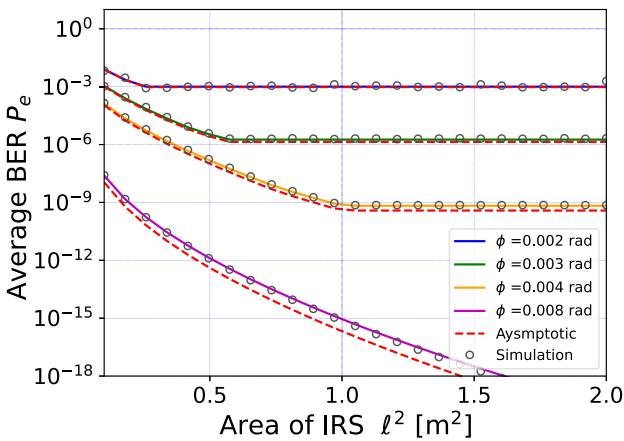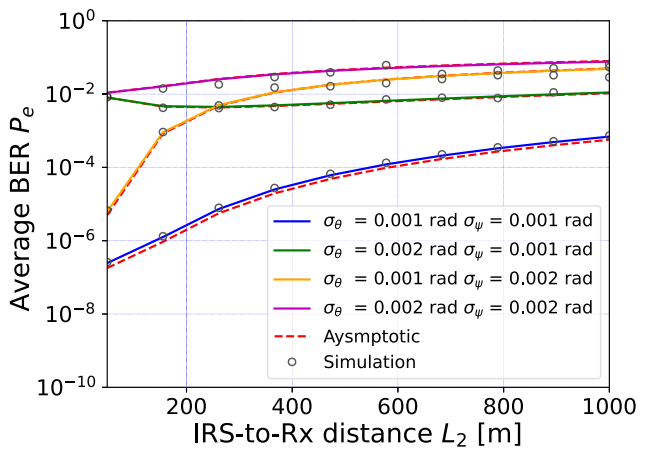

Fig. 10. Average BER in terms of IRS-to-Rx distance for different Tx and IRS jitters when Tx-to-IRS distance of 250 m and equal incident and reflection angles.

(a) $\sigma_\theta = 2 \times 10^{-3}$, $\sigma_\psi = 1 \times 10^{-3}$

(b) $\sigma_\theta = 1 \times 10^{-3}$, $\sigma_\psi = 2 \times 10^{-3}$
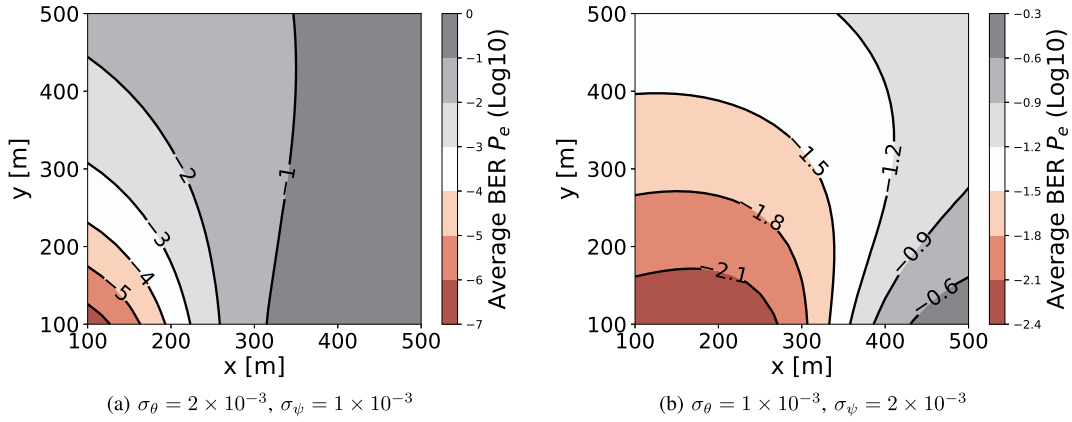
Fig. 11. Average BER as a function of IRS placement when the Tx and the Rx are placed at coordinates (0, 0) and (500, 0), respectively for different pointing errors.

(a) Different incident and reflection angles ($\theta_i \neq \theta_r$)

(b) Different incident and reflection angles ($\theta_i \neq \theta_r$) and infinite IRS size ($h_{irs} = 1$).

(c) Equal incident and reflection angles ($\theta_i = \theta_r$)

(d) Equal incident and reflection angles ($\theta_i = \theta_r$) and infinite IRS size ($h_{irs} = 1$).
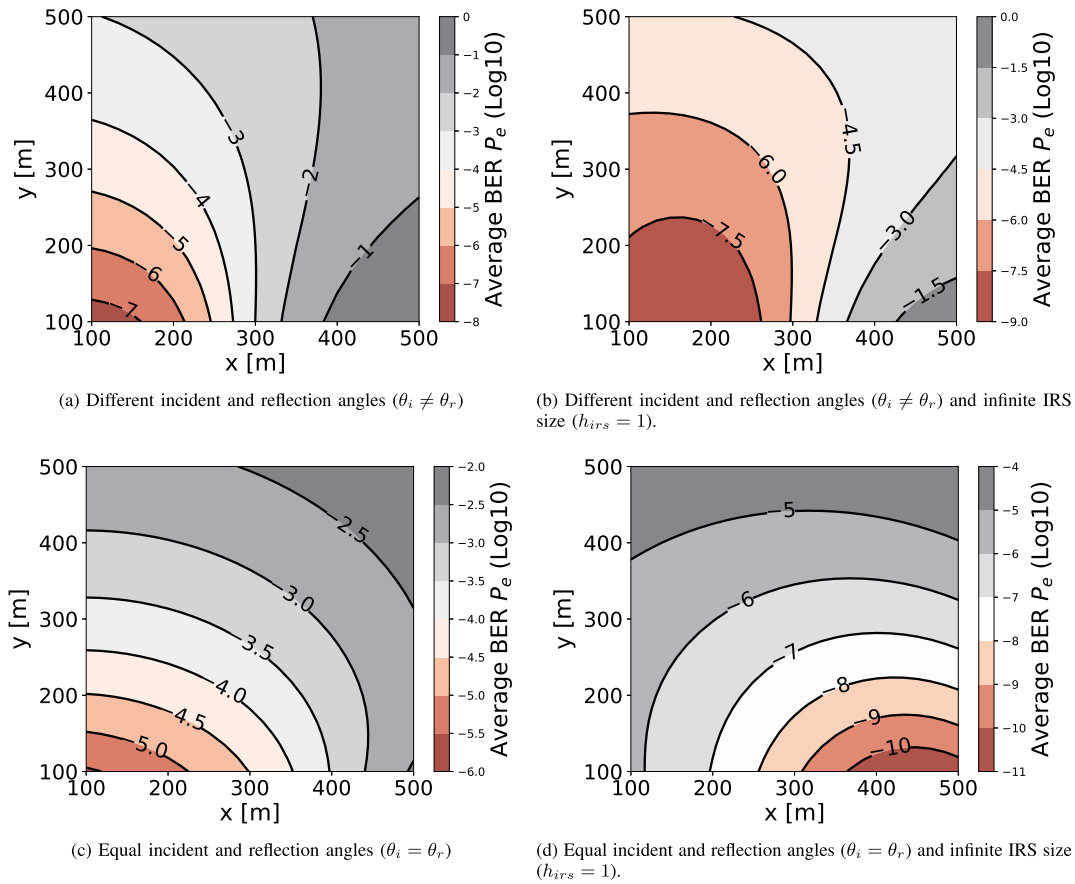
Fig. 12. Average BER performance as a function of IRS placement when the Tx is at coordinates (0, 0) and the Rx is at coordinates at (500, 0) under different scenarios.

less received power. Moreover, considering the impact of pointing error, the average BER decreases as the reflected beam is constrained by the smaller size of the IRS.

To further investigate the impact of the beam width, we evaluate the average BER in terms of the transmitted optical power for different beam widths in Fig. 6. From the figure, it can be seen that as the transmit divergence ϕ increases, the beam width expands. Subsequently, an enhancement in performance can be achieved as the beam width increases for various values of

ϕ, namely, $\phi = 0.002$ rad, $\phi = 0.004$ rad, and $\phi = 0.008$ rad. The widened beam contributes to a better alignment between the Tx and the Rx, thereby enhancing the system's robustness against the pointing errors. The curves corresponding to ψ values of 0.008 and 0.016 intersect at a transmitted optical power (P_t) of 17 dBm. Despite the larger beam width at $\phi = 0.016$ rad, resulting in reduced received signal power for an Rx radius of $a = 0.01$ m, the robustness against pointing errors is stronger than a narrower beam. In scenarios with low transmitted optical

power levels, enhanced performance is achieved with a narrower beam width, as the impact of signal attenuation outweighs that of pointing error.

The relationship between the average BER and the area of the IRS for different beam divergence angles is depicted in Fig. 7. Increasing the size of IRS areas typically enhances performance as it restricts optical beam reflection within the IRS surface. However, the improvement in average BER saturates at a specific threshold of the IRS areas depending on the beam divergence. For instance, saturation occurs when the square of the IRS side length (l^2) is greater than or equal to 0.55 m^2 for a beam divergence angle of 3×10^{-3} rad and when l^2 is greater than or equal to 1.0 m^2 for a beam divergence angle of 4×10^{-3} rad. Notably, saturation thresholds rise proportionally with the beam's divergence angle, necessitating a larger IRS to reflect optical beams with broader widths effectively.

To clarify the impact of the IRS design, we evaluate the outage probability as a function of IRS area for different spaces between adjacent IRS elements, denoted as z_a, as shown in Fig. 8. With an increase in z_a, the number of IRS elements within a designated area decreases, consequently limiting the available surface for reflecting optical beams. Thus, larger z_a values result in a degradation of system performance. As depicted in Fig. 8, when $z_a = 1$ cm, the outage probability $P_{out} = 10^{-12}$, whereas for $z_a = 3$ cm, $P_{out} = 10^{-11}$.

To assess the system design specifications regarding the positioning of the IRS relative to the Tx and Rx, the average BER performance is evaluated in Fig. 9, considering an IRS-to-Rx distance of 250 m, and in Fig. 10, considering a Tx-to-IRS distance of 250 m, while assuming equal incident and reflection angles. From Fig. 9, in scenarios with minimal pointing errors (i.e., $\sigma_\theta = 1 \times 10^{-3}$ rad and $\sigma_\psi = 1 \times 10^{-3}$ rad), it can be seen that increasing the distance between the Tx and IRS leads to improved robustness against pointing errors when utilizing a broader beam, aligning with expectations. Conversely, positioning the IRS closer to the Rx facilitates sufficient beam expansion, thereby enhancing robustness against pointing errors. On the other hand, the results depicted in Fig. 10 show that, under conditions where $\sigma_\theta = 2 \times 10^{-3}$ rad and $\sigma_\psi = 1 \times 10^{-3}$ rad, the average BER remains relatively stable due to a trade-off between robustness to pointing errors and other channel-degrading factors. However, in alternative scenarios, an increase in the IRS-to-Rx distance L_2 leads to deteriorating average BER due to the influence of factors degrading the channel. For instance, when $L_2 = 300$ m and $P_e = 5 \times 10^{-3}$, the average BER remains nearly constant irrespective of whether $\sigma_\theta = 2 \times 10^{-3}$ rad, $\sigma_\psi = 1 \times 10^{-3}$ rad or $\sigma_\theta = 1 \times 10^{-3}$ rad, $\sigma_\psi = 2 \times 10^{-3}$ rad. For $L_2 < 300$ m, superior performance is achieved under pointing error conditions where $\sigma_\theta < \sigma_\psi$, while for $L_2 > 300$ m, improvement is observed under conditions where $\sigma_\theta > \sigma_\psi$.

To assess the impact of pointing errors due to both Tx and IRS jitters, the average BER performance is assessed in terms of the IRS placement for different pointing errors in Fig. 11(a) and (b). In scenarios where Tx jitter surpasses IRS jitter ($\sigma_\theta = 2 \times 10^{-3}$ rad, $\sigma_\psi = 1 \times 10^{-3}$ rad), the results obtained in Fig. 11(a) show that positioning the IRS near the Tx yields superior performance. For example, achieving an average BER of 10^{-4} occurs when the

IRS is situated at (200, 150). Conversely, in scenarios where IRS jitter exceeds Tx jitter ($\sigma_\theta = 1 \times 10^{-3}$ rad, $\sigma_\psi = 2 \times 10^{-3}$ rad), optimal IRS placement tends towards the Rx side, as depicted in Fig. 11(b). For instance, an average BER of approximately 10^{-2} is achieved when the IRS is located within the region corresponding to $[100 \leq x \leq 250, y = 160]$. Notably, the impact of pointing errors increases when the IRS is positioned closer to the Rx, particularly for stronger IRS jitter.

Finally, Fig. 12(a)–(d) depict the average BER performance with respect to the IRS placement for two scenarios: equal and unequal incident and reflection angles. The Tx and Rx are positioned at coordinates $(0, 0)$ and $(500, 0)$, respectively, while the IRS location is denoted by coordinates (x, y) with $x, y \in [0, 500]$. Additionally, the system performance is assessed considering a single-element IRS size ($h_{irs} = 1$) for comparison, as depicted in Fig. 12(b) and (d). In Fig. 12(a), it is clear that placing the IRS in close proximity to the Tx enhances BER performance. For example, an average BER of 10^{-4} is achieved when $x < 280$ and $y < 370$. This proximity increases the link distance between the IRS and the Rx, resulting in a wider beam at the Rx. The broader beam enhances robustness against pointing errors, thus improving system performance. Moreover, smaller incident angles are preferred due to the reduced beam shifts caused by jitter. In Fig. 12(b), we can observe that although better performance is observed on the Tx side, it is not optimal close to the Tx due to link-dependent losses. In scenarios where incident and reflection angles are equal, system performance sees an improvement when the IRS is positioned near the Tx, as depicted in Fig. 12(c). For instance, achieving an average BER of 10^{-5} occurs when $x < 220$ and $y < 150$. Conversely, in cases where an infinite IRS size is assumed, enhanced performance is observed when the IRS is situated close to the Rx, as illustrated in Fig. 12(d).

IV. CONCLUSION

In this paper, we investigated the performance of a multi-link IRS-assisted terrestrial FSO system, considering pointing errors arising from both Tx and IRS jitter effects. We also investigated how the design and placement of the IRS influence system performance, offering guidelines for optimal IRS positioning. We presented a comprehensive mathematical model accounting for the main degrading factors such as Tx jitter, IRS jitter, incident angle, and reflection angle. Moreover, we derived closed-form expressions for average BER and outage probability. Based on our results, placing the IRS near the Tx while considering a finite IRS size leads to enhanced system performance regardless of whether incident and reflection angles align. Moreover, we showed that optimal IRS placement depends on both Tx and IRS jitter angles. Specifically, with increasing IRS jitter, optimal positioning tends to shift closer to the Rx side.

Hence, the presented analysis yields valuable insights into important considerations for the effective design of IRS-assisted FSO systems, highlighting the significance of addressing pointing errors and optimizing IRS placement to enhance performance.

REFERENCES

[1] A. Bekkali, M. Hattori, Y. Hara, and Y. Suga, "Free space optical communication systems for 6G: A modular transceiver design," *IEEE Wireless Commun. Mag.*, vol. 30, no. 5, pp. 50–57, Oct. 2023.

[2] C. B. Naila, K. Wakamori, M. Matsumoto, A. Bekkali, and K. Tsukamoto, "Transmission analysis of digital TV signals over a radio-on-FSO channel," *IEEE Commun. Mag.*, vol. 50, no. 8, pp. 137–144, Aug. 2012.

[3] H.-B. Jeon et al., "Free-Space optical communications for 6G wireless networks: Challenges, opportunities, and prototype validation," *IEEE Commun. Mag.*, vol. 61, no. 4, pp. 116–121, Apr. 2023.

[4] M. A. Khalighi and M. Uysal, "Survey on free space optical communication: A communication theory perspective," *IEEE Commun. Surveys Tuts.*, vol. 16, no. 4, pp. 2231–2258, Fourthquarter 2014.

[5] C. B. Naila, A. Bekkali, K. Wakamori, and M. Matsumoto, "Transmission analysis of CDMA-based wireless services over turbulent radio-on-FSO links using aperture averaging," in *Proc. IEEE Int. Conf. Commun.*, 2011, pp. 1–6.

[6] C. B. Naila, A. Bekkali, K. Wakamori, and M. Matsumoto, "Performance analysis of CDMA-based wireless services transmission over a turbulent RF-on-FSO channel," *IEEE/Optica J. Opt. Commun. Netw.*, vol. 3, no. 5, pp. 475–486, May 2011.

[7] A. Bekkali, C. B. Naila, K. Kazaura, K. Wakamori, and M. Matsumoto, "Transmission analysis of OFDM-based wireless services over turbulent radio-on-FSO links modeled by gamma-gamma distribution," *IEEE Photon. J.*, vol. 2, no. 3, pp. 510–520, Jun. 2010.

[8] A. A. Farid and S. Hranilovic, "Outage capacity optimization for free-space optical links with pointing errors," *J. Lightw. Technol.*, vol. 25, no. 7, pp. 1702–1710, Jul. 2007.

[9] M. R. Bhatnagar and Z. Ghassemlooy, "Performance analysis of Gamma-Gamma fading FSO MIMO links with pointing errors," *J. Lightw. Technol.*, vol. 34, no. 9, pp. 2158–2169, May 2016.

[10] L. Kong, W. Xu, L. Hanzo, H. Zhang, and C. Zhao, "Performance of a free-space-optical relay-assisted hybrid RF/FSO system in generalized M-distributed channels," *IEEE Photon. J.*, vol. 7, no. 5, Oct. 2015, Art. no. 7903319.

[11] W. Liu, J. Ding, J. Zheng, X. Chen, and C.-L. I., "Relay-assisted technology in optical wireless communications: A survey," *IEEE Access*, vol. 8, pp. 194384–194409, 2020.

[12] V. Jamali, H. Ajam, M. Najafi, B. Schmauss, R. Schober, and H. V. Poor, "Intelligent reflecting surface assisted free-space optical communications," *IEEE Commun. Mag.*, vol. 59, no. 10, pp. 57–63, Oct. 2021.

[13] M. Najafi, B. Schmauss, and R. Schober, "Intelligent reflecting surfaces for free space optical communication systems," *IEEE Trans. Commun.*, vol. 69, no. 9, pp. 6134–6151, Sep. 2021.

[14] S. Malik, P. Saxena, and Y. H. Chung, "Performance analysis of a UAV-based IRS-assisted hybrid RF/FSO link with pointing and phase shift errors," *J. Opt. Commun. Netw.*, vol. 14, no. 4, pp. 303–315, Apr. 2022.

[15] H. Ajam, M. Najafi, V. Jamali, B. Schmauss, and R. Schober, "Modeling and design of IRS-Assisted multilink FSO systems," *IEEE Trans. Commun.*, vol. 70, no. 5, pp. 3333–3349, May 2022.

[16] H. Wang et al., "Performance analysis of multi-branch reconfigurable intelligent surfaces-assisted optical wireless communication system in environment with obstacles," *IEEE Trans. Veh. Technol.*, vol. 70, no. 10, pp. 9986–10001, Oct. 2021.

[17] J. Sipani, P. Sharda, and M. R. Bhatnagar, "Modeling and design of IRS-assisted FSO system under random misalignment," *IEEE Photon. J.*, vol. 15, no. 4, Aug. 2023, Art. no. 7303113.

[18] J.-H. Noh and B. Lee, "Phase-shift design and channel modeling for focused beams in IRS-Assisted FSO systems," *IEEE Trans. Veh. Technol.*, vol. 72, no. 8, pp. 10971–10976, Aug. 2023.

[19] T. V. Nguyen, H. D. Le, and A. T. Pham, "On the design of RIS-UAV relay-assisted hybrid FSO/RF satellite-aerial-ground integrated network," *IEEE Trans. Aerosp. Electron. Syst.*, vol. 59, no. 2, pp. 757–771, Apr. 2023.

[20] H. Wang, Z. Zhang, B. Zhu, J. Dang, and L. Wu, "Performance analysis of hybrid RF-reconfigurable intelligent surfaces assisted FSO communication," *IEEE Trans. Veh. Technol.*, vol. 71, no. 12, pp. 13435–13440, Dec. 2022.

[21] V. K. Chapala and S. M. Zafaruddin, "Multiple RIS-Assisted mixed FSO-RF transmission over generalized fading channels," *IEEE Syst. J.*, vol. 17, no. 3, pp. 3515–3526, Sep. 2023.

[22] A.-A. A. Boulogeorgos, N. D. Chatzidiamantis, H. G. Sandalidis, A. Alexiou, and M. D. Renzo, "Cascaded composite turbulence and misalignment: Statistical characterization and applications to reconfigurable intelligent surface-empowered wireless systems," *IEEE Trans. Veh. Technol.*, vol. 71, no. 4, pp. 3821–3836, Apr. 2022.

[23] N. Vishwakarma, R. Swaminathan, P. D. Diamantoulakis, and G. K. Karagiannidis, "Performance analysis of optical reflecting surface-assisted optical space shift keying-based MIMO-FSO system," *IEEE Trans. Commun.*, vol. 71, no. 8, pp. 4751–4763, Aug. 2023.

[24] F. N. Igboamalu, A. R. Ndjiongue, and K. Ouahada, "Capacity analysis of an MISO free-space optical communications assisted by concave ORIS," *IEEE J. Commun. Inf. Netw.*, vol. 8, no. 3, pp. 295–302, Sep. 2023.

[25] H. Ajam, M. Najafi, V. Jamali, and R. Schober, "Power scaling law for optical IRSs and comparison with optical relays," in *Proc. IEEE Glob. Commun. Conf.*, 2022, pp. 1527–1533.

[26] H. Ajam, M. Najafi, V. Jamali, and R. Schober, "Optical IRSs: Power scaling law, optimal deployment, and comparison with relays," *IEEE Trans. Commun.*, vol. 72, no. 2, pp. 954–970, Feb. 2024.

[27] T. Ishida, C. B. Naila, H. Okada, and M. Katayama, "Performance analysis of intelligent reflecting surface assisted-FSO system over turbulent channels with pointing errors," in *Proc. IEEE Veh. Technol. Conf.*, 2023, pp. 1–5.

[28] Z. Ghassemlooy, W. Popoola, and S. Rajbhandari, *Optical Wireless Communications System and Channel Modelling With MATLAB*. Boca Raton, FL, USA: CRC Press, 2012.

[29] L. C. Andrews, R. L. Phillips, and C. Y. Young, *Laser Beam Scintillation With Applications*. Bellingham, WA, USA: SPIE, 2001.

[30] Wolfram functions. Accessed: Jun. 2019. [Online]. Available: https://functions.wolfram.com/PDF/MeijerG.pdf

[31] I. S. Gradshteyn and I. M. Ryzhik, *Table of Integrals, Series, and Products*, 6th ed. New York, NY, USA: Academic, 2000.

[32] V. S. Adamchik and O. I. Marichev, "The algorithm for calculating integrals of hypergeometric type functions and its realization in REDUCE system," in *Proc. Int. Conf. Symbolic Algebr. Comput.*, 1990, pp. 212–224.

[33] A. G. Zambrana et al., "Asymptotic error-rate analysis of FSO links using transmit laser selection over gamma-gamma atmospheric turbulence channels with pointing errors," *Opt. Exp.*, vol. 20, pp. 2096–2109, 2012.